Journal of Magnetic Resonance 307 (2019) 106578

Contents lists available at ScienceDirect

Journal of Magnetic Resonance

journal homepage: www.elsevier.com/locate/jmr

Three-dimensional MRI in a homogenous 27 cm diameter bore Halbach array magnet

T. O'Reilly, W.M. Teeuwisse, A.G. Webb *

C.J. Gorter Center for High Field MRI, Department of Radiology, Leiden University Medical Center, Leiden, the Netherlands

ARTICLE INFO

Article history:
Received 15 July 2019
Revised 15 August 2019
Accepted 16 August 2019
Available online 20 August 2019

Keywords:
Sustainable MRI
Halbach array
Low field MRI
Permanent magnets
Hydrocephalus

ABSTRACT

Modern clinical MRI systems utilise very high magnetic fields strengths to produce high resolution images of the human body. The high up-front and maintenance cost of these systems means that much of the world lacks access to this technology. In this paper we propose a low cost, head-only, homogenous Halbach magnet array with the potential for paediatric neuroimaging in low-resource settings. The homogeneity of the Halbach array is improved by allowing the diameter of the Halbach array to vary along its length, and also adding smaller internal shim magnets. The constructed magnet has a bore diameter of 27 cm, mean B_0 field strength of 50.4 mT and a homogeneity of 2400 ppm over a 20 cm diameter spherical volume. The level of homogeneity of the system means that coil-based gradients can be used for spatial encoding which greatly increases the flexibility in image acquisition. 3D images of a "brain phantom" were acquired over a 22 × 22 × 22 cm field of view with a 3.5 mm isotropic resolution using a spin-echo sequence. Future development of a low-cost gradient amplifier and an open-source spectrometer has the potential of offering a fully open-source, low-cost MRI system for paediatric neuroimaging in low-resource settings.

1. Introduction

The first MRI scanners produced in the 1980s had field strengths on the order of 0.1–0.5 Tesla. With improved magnet design and technology, human-sized superconducting magnets of 1.5 T and 3 T became commercially available, and most clinical research is performed at these field strengths. Typical purchase costs of a commercial MRI scanner are 1 million euros per Tesla [1], with annual service contracts of hundreds of thousands of euros, and a high level of expertise required for operation and repair, placing such systems completely out of reach for many communities [2]. Eliminating the superconducting magnet from the MRI system allows for a significant reduction in cost but comes with a large reduction in available magnetic field strength. The major problem with such low-field MRI systems is simply signal-to-noise ratio (SNR) which, in the low field limit, is proportional to the 7/4th power of B_0 [3], and while the this ratio tends towards linearity with increasing magnetic field strength reducing the magnetic field strength from a typical clinical strength of 1.5 T to ~50 mT (the field strength of the magnet described in this paper) comes with a several hundred fold reduction in SNR. However, there are also some distinct advantages of low-field MRI [4] including the ability to scan patients with implants and the fact that the power deposited is much lower, meaning that the specific absorption rate (SAR) which is determined by federal law, is in practice never reached.

The pioneering attempts at performing human MRI at low-fields used the concept of pre-polarized MRI, in which an inhomogeneous pulsed magnetic field could be used to polarize the nuclei, with the signal being read out in a more homogeneous lower magnetic field. In the 1990s the Stanford group [5] showed that this principle could be used for hand and wrist imaging. Many academic groups have developed unconventional detectors such as atomic magnetometers [6,7] and superconducting quantum devices (SQUIDs) [6,8–11] but these have remained in the academic arena. More recently, larger bore magnets have been produced with the aim of brain imaging. One example has been the Helmholz coil-based system used to acquire images of the human brain at 6.5 mT: images have been acquired at a spatial resolution of 2.5 × 3.5 × 8.5 mm^3 using balanced steady-state free-precession techniques [12]. This system has produced high quality human brain images at very low field. The only disadvantage is that its large size reduces the portability of the system, a facet which would prove useful in developing countries.

* Corresponding author at: C.J. Gorter Center for High Field MRI, Department of Radiology, Leiden University Medical Centre, Albinusdreef 2, 2333 ZA Leiden, the Netherlands.
E-mail address: a.webb@lumc.nl (A.G. Webb).

https://doi.org/10.1016/j.jmr.2019.106578
1090-7807/

The pioneering work of Blümler and associates [13–18] as well as Perlo, Casanova and Blümlich [19–22] highlighted the potential of a discretized version of a Halbach magnet, referred to as a Mandhala, to produce the main B_0-field using arrays of permanent magnets. Through a combination of very high length-to-bore ratios and the ability to finely tune the positions of the individual magnets in the Halbach arrays field homogeneities needed to perform high-resolution NMR were obtained. The application of Halbach arrays to in-vivo has been limited due to the increased inhomogeneity that arises when the length-to-diameter ratio decreases [23] which is a practical requirement when building systems with a bore size suitable for human imaging. Designs that build in a B_0-gradient in Halbach arrays as a spatial encoding method have been shown [24–26] but face technical challenges due to the high gradient strength that is required to overcome imperfections in the encoding field and may be slightly less flexible than systems that use conventional gradient based encoding since the gradient is a fixed feature of the magnet design.

The particular aim of our project is to construct a platform to image pediatric hydrocephalus in developing countries. As discussed extensively by Obungoloch et al. [27] and references therein hydrocephalus is one of the most common pediatric conditions which requires both neuroimaging and neurosurgery. The image spatial resolution can be much coarser than used for conventional neuro-MRI, with voxels on the order of $3 \times 3 \times 10$ mm sufficient for identifying fluid compartments for fenestration or drainage. Critical requirements for such a system include low upfront cost, realized by the earlier described reduction in magnet cost and lower demands on the RF and gradient amplifiers due to the relatively small size of the system, a reduced operational and maintenance cost by removing the need for cryogen cooling and using electronic components that can easily be replaced or repaired, (ideally) portability which will allow greater access to MR technology in remote regions as well as making citing of the system in fixed locations easier, and very simple data acquisition, e.g. a simple three-dimensional spin-echo pulse sequence requiring minimal planning in cases where highly trained radiologists are not available. One can think of other applications of this technology if these requirements are met; deployment to disaster regions and field hospitals and integration in to ambulances to reduce the time needed to acquire (initial) diagnostic images. Additionally, a size and cost reduction of the MRI system opens up non-human applications such as quality control on food products and water quality monitoring.

In this paper we set out to design a head-only, homogenous Halbach magnet array for imaging hydrocephalus in young children using conventional-gradient-based image reconstruction. The homogeneity of the magnet is improved by optimizing the radius of the Halbach cylinder along the length of the magnet. The choice was made to use smaller magnets than other Halbach designs with the aim of averaging out the inevitable manufacturing imperfections of each individual magnet: this also reduces the demands on the magnet enclosure in terms of structural strength and weight, and increases safety during the construction process.

2. Method

2.1. Magnet design

The minimum bore size is determined by the width of the shoulders that need to be accommodated; in this magnet design we chose a bore diameter of 27 cm which is sufficiently large to accommodate the majority of the target population of paediatric patients up to the age of 8.

The main trade-offs to consider in the magnet design are the magnetic field homogeneity, the absolute value of the magnetic field, and the weight and the cost of the total assembly. As discussed in several previous publications [28–30] the major source of inhomogeneity is the finite length of the Halbach array, and so as many rings as possible should be used, with the obvious penalty of increased weight and cost. Also the larger the number of layers of magnets that are used the stronger the magnetic field, but again the higher the weight and cost.

As discussed in the introduction we chose to use smaller magnets ($12 \times 12 \times 12$ mm^3) than have been used in other designs, and together with the weight of the plastic (polymethylmethacrylate, PMMA) sheets used to house the magnets, this resulted in a total number of magnets of ~3000. Additionally we decided to use an approximate length:diameter ratio of 2:1 as a compromise between homogeneity and weight, but to use reduced-diameter rings at each end of the array to improve the homogeneity.

Using these constraints the magnet was designed with 23 circular Halbach rings spaced 22 mm apart, with a total magnet length of 50.6 cm. Each ring of the Halbach array consists of two concentric layers of $12 \times 12 \times 12$ mm^3 N48 neodymium boron iron (NdBFe) magnets (www.supermagnete.nl, 0.72 euros per magnet) arranged in a dipolar (k = 1) Halbach configuration [14] with the outer ring containing 7 more magnets and having a 20 or 21 mm larger radius (see Fig. 1a)).

In order to optimize the field homogeneity, the diameter of each ring was allowed to vary from 296 to 442 mm, while the spacing between magnets in the rings was kept constant for all ring diameters. Halbach rings with 50–75 magnets (148–221 mm radius, respectively) were simulated using the magnetostatic solver in CST Studio Suite 2017 (Dassault Systèmes, Vélizy-Villacoublay, France).

The magnetic field map of each of the Halbach rings was exported with a $2 \times 2 \times 2$ mm^3 resolution and read into a customized programme written in Python 3.7. The radius of each of the layers of the Halbach array was subsequently optimised for homogeneity over a 25 cm diameter spherical volume (DSV) placed at the isocentre of the magnet using the genetic algorithm (GA) in the Distributed Evolutionary Algorithms in Python (DEAP) package [31] by minimising the inhomogeneity of the magnet:

$$f_{cost} = \frac{max(B_z(r)) - min(B_z(r))}{mean(B_z(r))} \quad (1)$$

The genetic algorithm was run for 250 generations with a population size of 25,000. The top 5% of configurations with the lowest cost functions were cloned to the next generation, 55% of the following generation were created using the cross-over operator and 45% with the mutation operator. Symmetry of the ring diameters about the isocentre of the Halbach array was enforced to maximize homogeneity and reduce the size of the solution space.

The result of the GA optimization was simulated in CST microwave Studio to verify the results. The outer ring of the middle layer of the Halbach array was manually adjusted to be 1 step larger (75 as opposed to 74 magnets) to correct for a small increase in the B_0 field towards the centre of the magnet observed in simulations. A side view of the optimised magnet configuration is shown in Fig. 1(b), the specifications of each ring in the Halbach array are given in Table 1.

2.2. Magnet construction

To construct the optimized design each ring of the Halbach array was constructed separately using 4 sheets of laser-cut PMMA held together using M3 brass nuts and bolts. Two 6 mm thick sheets of extruded PMMA were used to hold the magnets in place and a 3 mm thick sheet of extruded PMMA on either side functioned as a lid. Due to the limited size of the laser cutter bed the

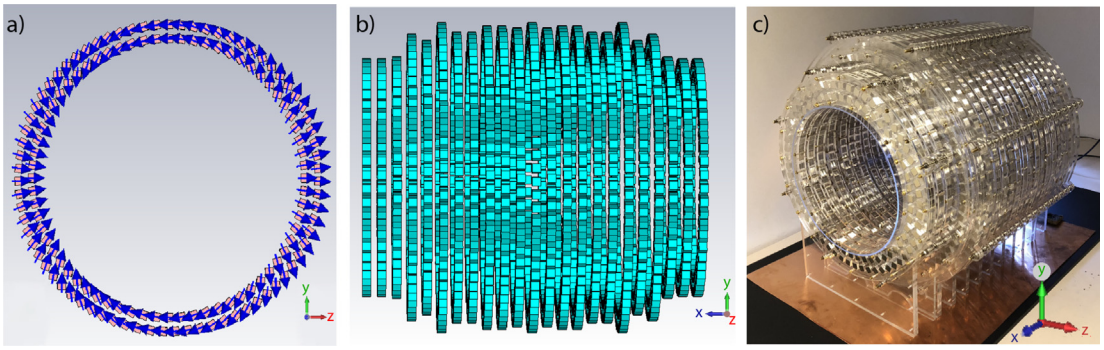

Fig. 1. (a) Two layers of magnets are used in each Halbach array layer. The magnetic field points in the +Z-direction, across the bore, the main axis of the cylinder lies along the +X-axis. (b) A side view of the Halbach array optimised for homogeneity by varying the diameter of each ring. The ring diameters used in the magnet design are symmetric about the isocenter of the Halbach array. (c) The constructed Halbach array based on the optimised Halbach configuration. Each ring is constructed separately using PMMA holders and fixed together using threaded brass rods.

Table 1
Configuration of magnets within the individual rings of the 27 cm inner diameter Halbach array, note the symmetry of the Halbach array design about the center ring, ring number 12. The spacing between the centre of each ring is 22 mm. A total number of 2948 cuboid N48 neodynium iron boron magnets are used.

Ring number	Inner layer Radius (mm)	Inner layer Number of magnets	Outer layer Radius (mm)	Outer layer Number of magnets
1&23	148	50	168	57
2&22	148	50	168	57
3&21	151	51	171	58
4&20	183	62	204	69
5&19	174	59	195	66
6&18	201	68	221	75
7&17	186	63	207	70
8&16	186	63	207	70
9&15	195	66	216	73
10&14	195	66	216	73
11&13	192	65	213	72
12	198	67	221	75

PMMA sheets for the inner 17 rings had to be cut in two separate segments. The completed layers were positioned using eight M5 brass threaded-rods located on the outside of the magnet. The three smaller Halbach array rings on either end of the magnet could easily be removed to facilitate the placement of additional components inside the bore. Fig. 1(c) shows a photograph of the final constructed magnet. The material cost of the constructed magnet was approximately 4000 euros. In order to maintain the possibility of having the magnet as a portable device, we limited the weight to ~75 kg of which 39 kg was contributed by the magnets and 36 kg was the plexiglass holders.

2.3. Magnetic field measurement and additional shimming

A 3D B_0 field map with a resolution of $5 \times 5 \times 5\ mm^3$ was acquired using an Alphalab inc. GM2 magnetometer with the High Stability Universal Probe (Salt Lake City, UT, United States) mounted on a 3-axis robotic positioning system [32].

After the B_0 map was analyzed shimming was implemented using additional $3 \times 3 \times 3\ mm^3$ N45 NdBFe magnets placed inside the magnet. A 325 mm diameter cylindrical grid of potential magnet positions, consisting of 15 layers spaced 15 mm apart with 60 potential magnet position in each layer, was defined. Each position had three options; no magnet, the magnetic moment oriented in the k = 1 Halbach direction, or rotated 180 degrees from this orientation. This orientation was found to perform better in simulations compared to having the fields of the magnets pointing radially (k = 0 configuration). The magnetic field of the shim magnets was calculated by approximating the magnets as magnetic dipoles:

$$\vec{B}(r) = \frac{\mu_0}{4\pi}\left[\frac{3\,\vec{r}(\vec{m}\cdot\vec{r})}{r^5} - \frac{\vec{m}}{r^3}\right] \tag{2}$$

where $\vec{m}$ is the magnetic moment of the magnet. The occupation of the grid was optimised using the same genetic algorithm as for the magnet design with the modified cost function minimising the B_0 range over a 20 cm DSV:

$$f_{cost} = max(B_z(r)) - min(B_z(r)) \tag{3}$$

The measured B_0 map was used as the input to the genetic algorithm. The algorithm was run for 250 generations with a population size of 25,000. The top 5% of configurations with the lowest cost functions were cloned to the next generation, 75% of the following generation were created using the cross-over operator and 20% with the mutation operator. The optimised shim configuration occupied a total of 644 magnets out of a possible 900 places in which a magnet could be placed, of which 408 magnets are in the k = 1 orientation and 236 are rotated 180 degrees from this orientation. The total cost of the shim magnets was 80 euros. The shim magnets are placed in plexiglass holders with an inner diameter of 315 mm and does not affect the bore size of the magnet.

2.4. Gradient coil design and construction

Quadrupolar Y and Z gradients were constructed as described in [33,34] with a 10/7 winding pattern. The gradients were 29 cm long, had an outer diameter 25 cm, and were printed with a 2 mm trace on 0.1 mm-thick flexible PC board. The inductance

and resistance of both gradients was measured to be 203 μH and 10.0 Ω, respectively with a gradient efficiency of 2.2 mT/m/A. A photograph of the gradients is shown in Fig. 2(a). The X-gradient was designed using a target field approach [35]. It was constructed using 14 turns per quadrant with 3 layers of 0.8 mm diameter enamelled copper wire per turn with a total coil length of 350 mm and a diameter of 272 mm, and is shown in Fig. 2(b). The inductance and resistance of the X gradient coil were 1.38 μH and 3.9 Ω, respectively, with a gradient efficiency of 1.4 mT/m/A. Simulations carried out in CST Microwave Studio show that the linearity over a 20 cm diameter-of-spherical is better than 10% for the Y and Z gradients, and better than 20% for the X gradient. No active cooling of the gradient coils was used. Photographs of the three gradient sets are shown in Fig. 2.

The gradients were driven using AE Techron 7224 amplifiers (Elkhart, IN, USA). Sixth order Butterworth filters (f_c = 100 kHz, Z_{in} = 1 Ω, Z_{out} = 1 Ω) were placed on the gradient lines to reduce RF noise introduced by the gradient amplifiers and gradient lines entering the Faraday cage.

2.5. Radiofrequency coil

The RF coil was an 18-turn solenoid, length 29 cm, diameter 20 cm, constructed from 1 cm wide copper tape. The coil was segmented half-way along its length with a 250 pF capacitor. Impedance matching to 50 Ω at 2.15 MHz was performed with a parallel capacitance of 230 pF and series capacitance of 690 pF. A Faraday shield consisting of a copper sheet with thickness 35 μm was placed on the inside of the Y gradient coil, approximately 2 cm from the solenoid. The quality factor (Q-factor) was measured with a vector network analyser to be 14 giving a FWHM of 154 kHz (note that the relatively low Q-factor is dictated by the equivalent series resistance of the high-loss non-magnetic capacitors). A custom built 1 kW RF amplifier with 60 dB gain was used to amplify the RF pulse from the spectrometer.

2.6. RF shielding

To minimize the environmental noise the entire setup was placed inside a 62.5 × 62.5 × 85 cm^3 Faraday cage constructed from 2 mm thick aluminium sheets and 32 × 32 mm^2 aluminium extrusion profiles.

2.7. Data acquisition

A Magritek Kea2 spectrometer (Aachen, Germany) was used for data acquisition. Two-dimensional images were acquired using a spin-echo sequence with the following parameters: repetition time (TR): 600 ms, echo time (TE): 15 ms, data matrix: 128 × 128 complex points, field-of-view: 200 × 200 mm^2, no slice selection, pulse duration: 130 μs, acquisition bandwidth: 33 kHz, 4 signal averages. Three-dimensional images were acquired using a 3D spin echo sequence with the following parameters: TR: 500 ms, TE: 30 ms, data matrix: 64 × 64 × 64 complex points, field-of-view: 220 × 220 × 220 mm^3, pulse durations: 130 μs, acquisition bandwidth: 20 kHz, one signal average. All data were filtered using a Gaussian filter:

$$f(k_x, k_y, k_z) = e^{-\frac{6k_x^2}{n_{k_x}}} e^{-\frac{6k_y^2}{n_{k_y}}} e^{-\frac{6k_z^2}{n_{k_z}}} \quad (4)$$

with n_{k_x}, n_{k_y} and n_{k_z} the number of acquired k space points in the x, y and z direction, respectively.

2D images were acquired of a "geometric" phantom consisting of 37 tubes of water (each of diameter 1.5 cm, length 9.5 cm, filled with water doped with Gd-DTPA to give a T_1 values of 160 ms) arranged hexagonally: the total dimensions of the phantom were 19 cm × 19 cm. 3D images were acquired on a "brain contrast phantom" consisting of an avocado placed inside a watermelon to provide internal contrast and a geometry somewhat related to the in-vivo brain. T_1 values were measured with an inversion-recovery sequence with eight inversion times, and T_2 values with a Carr-Purcell-Meiboom-Gill sequence with 32 echoes.

3. Results

Fig. 3 shows the simulated magnetic field distribution of the optimised Halbach ring configuration generated by the genetic algorithm. The B_0 field at the centre of the magnet was simulated to be 50.67 mT with a B_0 homogeneity over a 20 cm DSV (marked by the white dotted line) of 440 ppm.

Fig. 4(a) shows the magnetic field measured with the Hall probe and the three-dimensional robotic positioner with the same field-of-view as the simulations shown in Fig. 3. The homogeneity over the same 20 cm DSV used in simulations, 13,000 ppm, was significantly worse than the value simulated in Fig. 3. It was observed that warping of the plexiglass rings holding the magnets in place occurred during the construction process causing errors in the positions of the magnets that exceeded 1 mm in certain places and is the likely cause for the deteriorated homogeneity of the constructed magnet compared to simulations. The effect of variations in the magnetic field strength of the individual magnets in the Halbach array of up to ±1% was studied using simulations and found to only contribute a few 100 ppm to the inhomogeneity of the system and is therefore unlikely to be the main contributor to the decreased homogeneity.

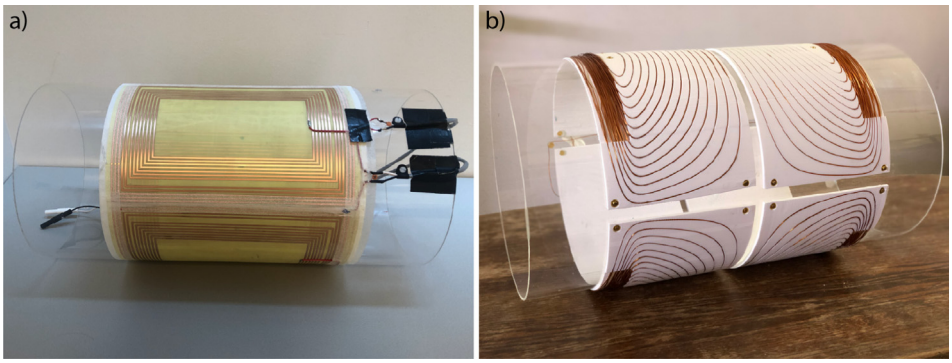

Fig. 2. (a) Y- and Z-gradient sets consisting of flexible printed circuit boards placed on a PMMA cylinder. The two gradients were rotated 45° with respect to one another. (b) X-gradient with the wire patterns derived from a target-field approach.

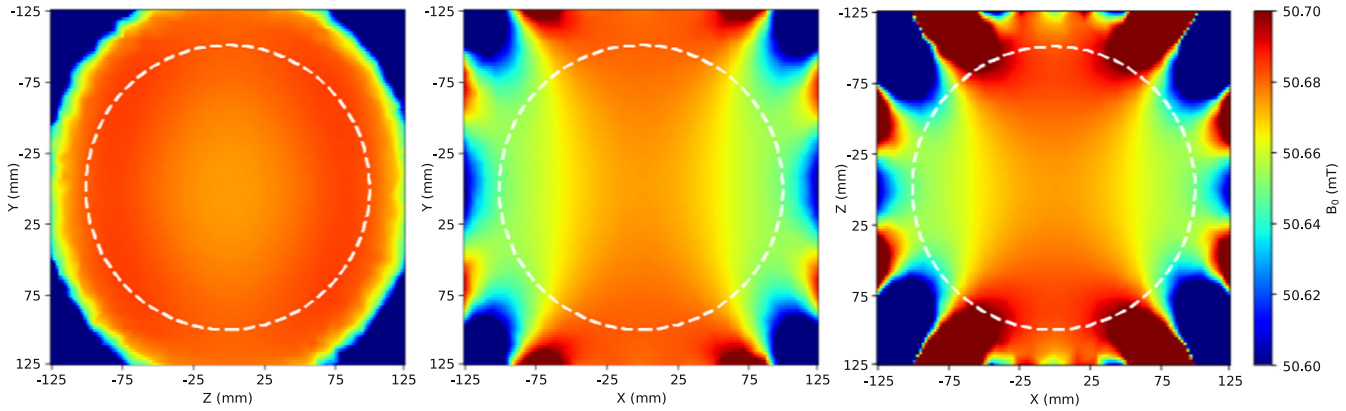

Fig. 3. Simulated magnetic field distribution of the Halbach array optimised for maximum homogeneity. The bore of the magnet lies along the X axis and the B_0 field along the Z axis.

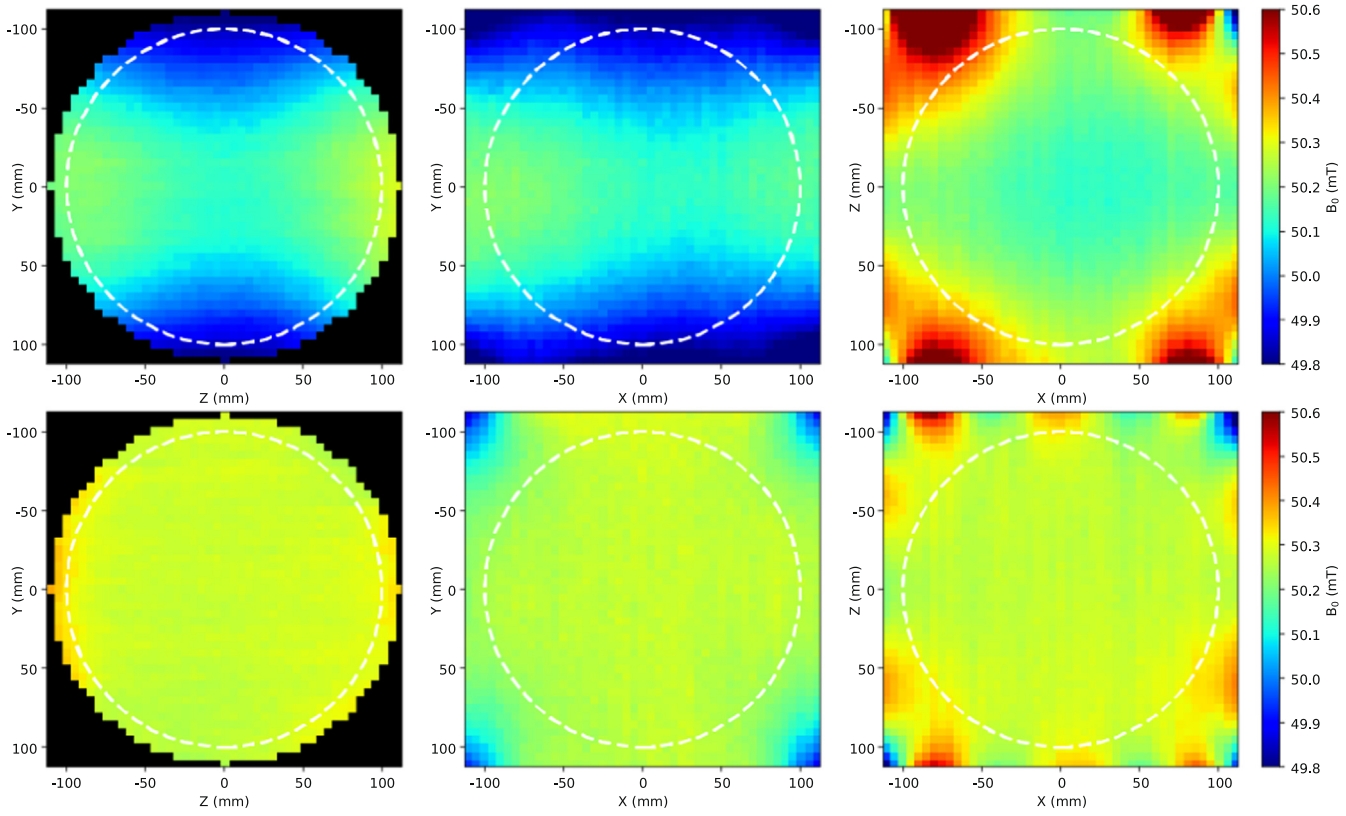

Fig. 4. (Top) Measured B_0 maps of the constructed magnet along 3-planes (see Fig. 1). Homogeneity over a 20 cm DSV (marked by the white dotted line) was measured to be 13,000 ppm. (Bottom) Measured B_0 maps after a single iteration of shimming using 3 mm cuboid N45 magnets arranged in a cylindrical grid. The filling of the grid was optimised using a genetic algorithm. Homogeneity over the same 20 cm DSV improved to 2486 ppm.

Based on the measured B_0 maps additional shim rings were designed as described in the Methods section and added to the inside of the magnet. Fig. 4(b) shows the considerable improvements made by these shim rings, with the larger patterns of inhomogeneity in Fig. 4(a) largely resolved, and the homogeneity improved by approximately a factor-of-five to 2498 ppm over the same 20 cm DSV. Fig. 5 displays the B_0 field distribution before and after shimming, showing not only the significant improvement in the homogeneity of the system but also a slight increase in the magnetic field strength.

Fig. 6 shows spin-echo NMR spectra acquired with no data filtering from different sized samples placed in the centre of the shimmed magnet. Although the lines were not absolutely symmetric, the approximate full-width-half-maximum values were 150 Hz (4 cm sphere), 500 Hz (9 cm sphere) and 800 Hz (19 cm sphere).

Fig. 7(a) shows the 2D image acquired from the hexagonal phantom. The images show that there are some spatial distortions at the outside of the 19 cm diameter phantom (which could potentially be corrected using information from simulated or measured gradient fields). Fig. 7(b) shows a plot of the image intensity along the line drawn in Fig. 7(b). The phantoms show a relatively consistent width with only the outer most phantoms showing any broadening: the additional drop off in intensity can be attributed to RF inhomogeneity from the solenoid coil.

Fig. 8 shows three-dimensional images of the phantom consisting of an avocado placed within a watermelon. The respective T_1

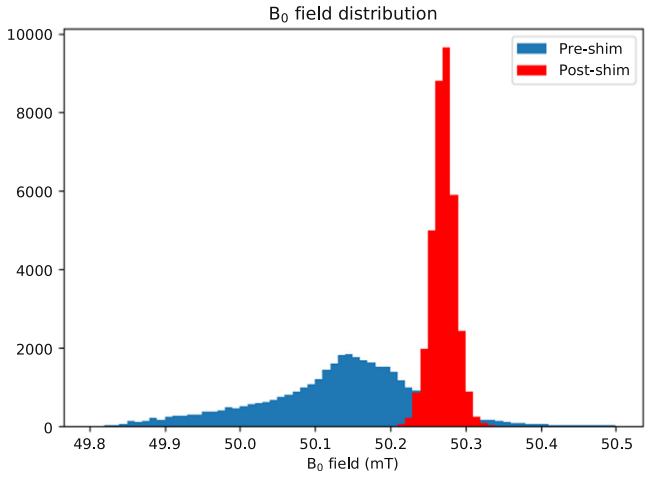

Fig. 5. B_0 field distribution over a 20 cm diameter spherical volume at the center of the Halbach array before and after shimming using additional 3 mm N45 cuboid magnets placed inside the bore of the Halbach array.

values were measured to be 340 ms and 1150 ms, and the T_2 values 170 ms and 600 ms. A relatively short repetition time (500 ms) was chosen to introduce T_1-contrast and also to keep the data acquisition time to a reasonable time.

4. Discussion

There are several potential improvements to the system which are being investigated.

One of the disadvantages of using permanent magnet material is the temperature dependence of the magnetic field. In the case of N48 NdBFe magnets, the dependence is −0.12%/°C, corresponding to a field drift of −2.5 kHz per degree temperature increase. Heat produced by the gradient system has the potential to cause a drift in the magnetic field strength. In order to see if this shift is significant in terms of image reconstruction, we measured spectra before and after imaging using the same 3D sequence described in the method section. The frequency shift was ∼100 Hz, with almost no change in spectral line shape. For an imaging pixel bandwidth of 312 Hz, as used in Fig. 8, this means that there is less than one pixel drift over the time of the image acquisition. Using additional magnetic material with a different temperature coefficient can be used to compensate for temperature drift but will reduce the magnetic field of the system [22]. A method that can be incorporated in to the current design is to correct for potential blurring introduced by B_0 drift by recording spectra intermittently during data acquisition, and then apply the corresponding phase shift to the k-space data in post processing. This, of course, assumes that the spectral shift is the same throughout the entire field-of-view,

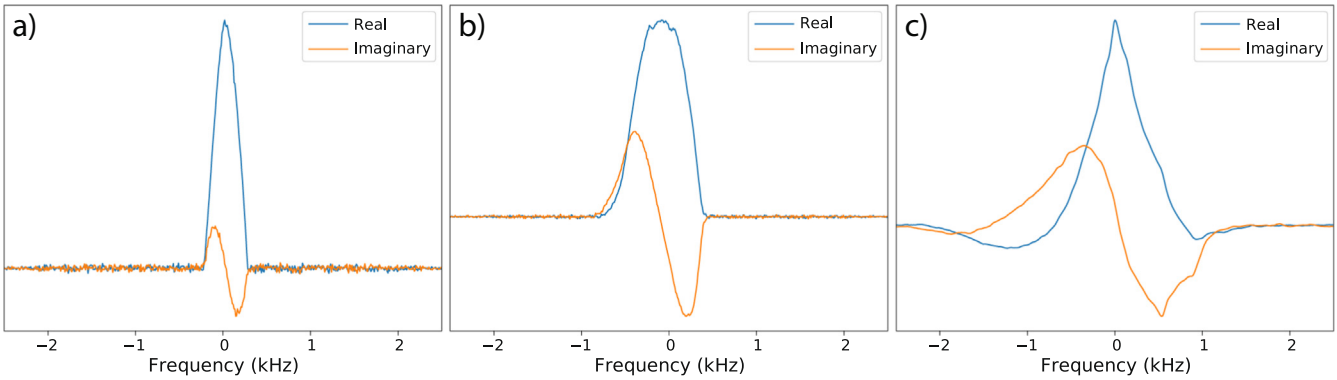

Fig. 6. Spectra from (a) 4 cm diameter sphere of water, (b) 9 cm diameter sphere of water, and (c) 19 cm diameter sphere of water. Data was acquired using a spin echo sequence with a spectral width of 5 kHz and 512 complex data points.

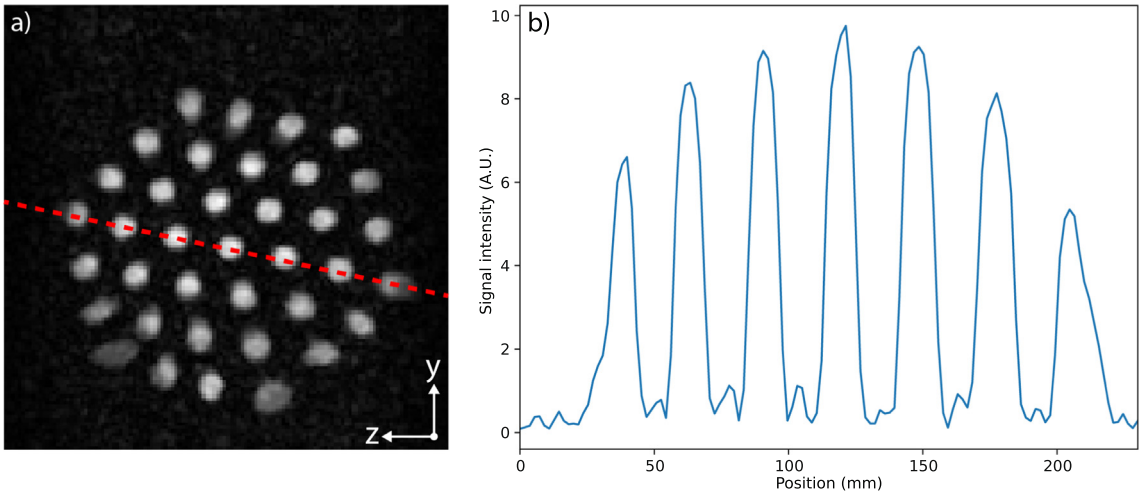

Fig. 7. (a) Image from the 37 tube geometric phantom data were acquired using a 2D spin echo sequence with a 1.6 × 1.6 mm in-plane resolution with an acquisition time of 10 min. (b) Image intensity plot along the red line in figure (a) showing some minor blurring of the outer-most phantoms. (For interpretation of the references to color in this figure legend, the reader is referred to the web version of this article.)

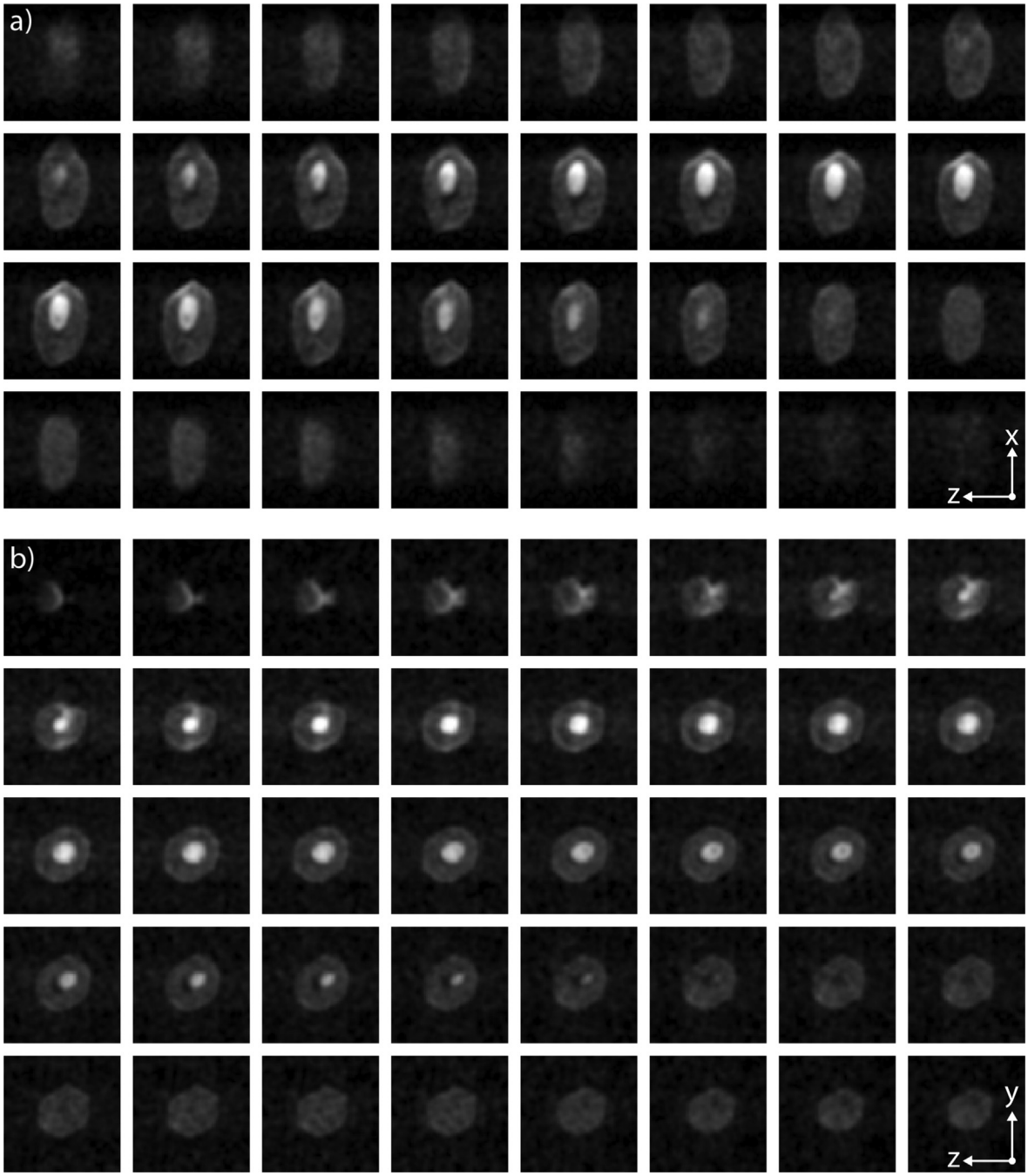

Fig. 8. Images from the 3D data set acquired at a spatial resolution of ~3.5 × 3.5 × 3.5 mm. The images are T1-weighted producing higher signal intensity from the inner avocado in comparison with the outer watermelon. Total data acquisition time ~34 min.

which is empirically supported by the similarity in pre- and post-experiment line shape. Multi-element temperature monitoring could easily be incorporated if more sophisticated image correction is required.

From an RF point-of-view, the current set-up uses a single coil for both transmit and receive. Other groups have demonstrated the use of multiple receive elements at low field [24]. There are several potential advantages of this approach including the use of parallel reconstruction techniques to reduce the imaging time (if the SNR is high enough to allow this), as well as the use of preamplifier decoupling to effectively widen the bandwidth of the coils during receive. In addition there may also be advantages to increasing the number of transmit channels, which would allow the use of higher efficiency class D switched mode amplifiers, which could be made much smaller, more modular and more easily replaceable [36].

The gradients described in this paper have very high resistances and inductances, which can be reduced using thick copper wire (rather than PC boards) and by using the target field approach for all three designs. In addition, one of the concerns at low-field is the role of concomitant gradients which can reduce the effective spatial resolution and introduce image distortions. As discussed by previous authors [37,38] any potential effects are largely mitigated by the use of spin-echo imaging sequences: however, one can potentially introduce minimization of concomitant gradients into the target field approach cost function.

Two of the hardware subsystems in this work are commercial, the gradient amplifiers and the MR data acquisition console. Having determined the characteristics of the constructed gradient coils, and the current requirements to acquire specific spatial resolutions given the overall homogeneity of the magnet, our next step will be to design a custom 3-channel gradient amplifier capable of delivering up to 30 amps for a cost on the order of $1000–2000. The second aim is to design a new console based on low-cost hardware such as software defined radios (SDR) or similar architecture [39–43] and open source software. Essentially such a system would simply be required to send out a series of pulses (RF pulses, gradient pulses, TTL pulses for amplifier blanking/unblanking) and time-synchronized data acquisition. These developments would also open up possibilities of expanding the number of transmit and receive channels.

There are also several sequence-based improvements that will be investigated to reduce the imaging time and/or increase the SNR. Given the relatively long T_2 relaxation times at low field, particularly for very mobile species such as CSF in which the T_2 value is very similar to the T_1, RARE sequences [44] can be used to reduce the data acquisition time considerably. The lack of SAR concerns at low field strengths due to the low Larmor frequency means that short echo times and long echo trains can be used. Alternatively, CPMG sequences could be used to increase the SNR by echo addition for each phase encoding step. The only disadvantage of such an approach is that gradient coil heating might be increased, which would produce larger shifts in the main magnetic field than have currently been measured, and so the trade-offs between SNR, imaging time and magnet drift need to be carefully determined.

5. Conclusion

This work has shown the feasibility of performing three-dimensional MRI using a custom-designed low-cost, high-homogeneity Halbach magnet. Images have been acquired at a spatial resolution of a few millimeters within a data acquisition time of tens of minutes with a SNR of ~35 after matched filtering has been applied. Many of the components of this system have been custom-built, and future work will aim to replace the remaining commercial components by custom-designed ones to further the aim of producing a low-cost, sustainable MR system for the developing world.

Acknowledgements

This work was supported by Horizon 2020 European Research Grant FET-OPEN 737180 Histo MRI, Horizon 2020 ERC Advanced NOMA-MRI 670629, Simon Stevin Meester Prize and NWO WOTRO Joint SDG Research Programme W 07.303.101. We are grateful to Drs. Martin van Gijzen and Rob Remis at the TU Delft for collaborative discussions, and Danny de Gans at the TU Delft for construction of the RF amplifier.

References

[1] L. Glover, Why Does an MRI Cost So Darn Much?, Money, n.d. http://money.com/money/2995166/why-does-mri-cost-so-much/ (accessed June 24, 2019).
[2] WHO, Global Maps for Diagnostic Imaging, WHO, n.d. https://www.who.int/diagnostic_imaging/collaboration/global_collab_maps/en/ (accessed June 26, 2019).
[3] W.A. Edelstein, G.H. Glover, C.J. Hardy, R.W. Redington, The intrinsic signal-to-noise ratio in NMR imaging, Magn. Reson. Med. 3 (1986) 604–618, https://doi.org/10.1002/mrm.1910030413.
[4] J.P. Marques, F.F.J. Simonis, A.G. Webb, Low-field MRI: An MR physics perspective, J. Magn. Reson. Imag. 49 (2019) 1528–1542, https://doi.org/10.1002/jmri.26637.
[5] A. Macovski, S. Conolly, Novel approaches to low-cost MRI, Magn. Reson. Med. 30 (1993) 221–230, https://doi.org/10.1002/mrm.1910300211.
[6] I. Savukov, T. Karaulanov, Magnetic-resonance imaging of the human brain with an atomic magnetometer, Appl. Phys. Lett. 103 (2013), https://doi.org/10.1063/1.4816433.
[7] I. Savukov, T. Karaulanov, Anatomical MRI with an atomic magnetometer, J. Magn. Reson. 231 (2013) 39–45, https://doi.org/10.1016/j.jmr.2013.02.020.
[8] A.N. Matlashov, L.J. Schultz, M.A. Espy, R.H. Kraus, I.M. Savukov, P.L. Volegov, C. J. Wurden, SQUIDs vs. induction coils for ultra-low field nuclear magnetic resonance: experimental and simulation comparison, IEEE Trans. Appl. Supercond. 21 (2011) 465–468, https://doi.org/10.1109/TASC.2010.2089402.
[9] R. McDermott, S. Lee, B. ten Haken, A.H. Trabesinger, A. Pines, J. Clarke, Microtesla MRI with a superconducting quantum interference device, PNAS 101 (2004) 7857–7861, https://doi.org/10.1073/pnas.0402382101.
[10] V.S. Zotev, A.N. Matlachov, P.L. Volegov, H.J. Sandin, M.A. Espy, J.C. Mosher, A.V. Urbaitis, S.G. Newman, R.H. Kraus, Multi-channel SQUID system for MEG and ultra-low-field MRI, IEEE Trans. Appl. Supercond. 17 (2007) 839–842, https://doi.org/10.1109/TASC.2007.898198.
[11] V.S. Zotev, A.N. Matlashov, P.L. Volegov, A.V. Urbaitis, M.A. Espy, R.H.K. Jr, SQUID-based instrumentation for ultralow-field MRI, Supercond. Sci. Technol. 20 (2007) S367–S373, https://doi.org/10.1088/0953-2048/20/11/S13.
[12] M. Sarracanie, C.D. LaPierre, N. Salameh, D.E.J. Waddington, T. Witzel, M.S. Rosen, Low-cost high-performance MRI, Sci. Rep. 5 (2015) 15177, https://doi.org/10.1038/srep15177.
[13] P. Blümler, F. Casanova, CHAPTER 5: hardware developments: halbach magnet arrays, in: Mobile NMR and MRI, 2015, pp. 133–157, https://doi.org/10.1039/9781782628095-00133.
[14] H. Raich, P. Blümler, Design and construction of a dipolar Halbach array with a homogeneous field from identical bar magnets: NMR Mandhalas, Conc. Magn. Reson. Part B: Magn. Reson. Eng. 23B (2004) 16–25, https://doi.org/10.1002/cmr.b.20018.
[15] H. Soltner, P. Blümler, Dipolar Halbach magnet stacks made from identically shaped permanent magnets for magnetic resonance, Conc. Magn. Reson. Part A 36A (2010) 211–222, https://doi.org/10.1002/cmr.a.20165.
[16] C.W. Windt, H. Soltner, D. van Dusschoten, P. Blümler, A portable Halbach magnet that can be opened and closed without force: the NMR-CUFF, J. Magn. Reson. 208 (2011) 27–33, https://doi.org/10.1016/j.jmr.2010.09.020.
[17] C. Bauer, H. Raich, G. Jeschke, P. Blümler, Design of a permanent magnet with a mechanical sweep suitable for variable-temperature continuous-wave and pulsed EPR spectroscopy, J. Magn. Reson. 198 (2009) 222–227, https://doi.org/10.1016/j.jmr.2009.02.010.
[18] P. BlüMler, Proposal for a permanent magnet system with a constant gradient mechanically adjustable in direction and strength, Conc. Magn. Reson. Part B: Magn. Reson. Eng. 46 (2016) 41–48, https://doi.org/10.1002/cmr.b.21320.
[19] J. Perlo, F. Casanova, B. Blümich, 3D imaging with a single-sided sensor: an open tomograph, J. Magn. Reson. 166 (2004) 228–235, https://doi.org/10.1016/j.jmr.2003.10.018.
[20] E. Danieli, J. Mauler, J. Perlo, B. Blümich, F. Casanova, Mobile sensor for high resolution NMR spectroscopy and imaging, J. Magn. Reson. 198 (2009) 80–87, https://doi.org/10.1016/j.jmr.2009.01.022.
[21] E. Danieli, J. Perlo, B. Blümich, F. Casanova, Small magnets for portable NMR spectrometers, Angew. Chem. Int. Ed. 49 (2010) 4133–4135, https://doi.org/10.1002/anie.201000221.
[22] E. Danieli, J. Perlo, B. Blümich, F. Casanova, Highly stable and finely tuned magnetic fields generated by permanent magnet assemblies, Phys. Rev. Lett. 110 (2013) 180801, https://doi.org/10.1103/PhysRevLett. 110.180801.
[23] K. Turek, P. Liszkowski, Magnetic field homogeneity perturbations in finite Halbach dipole magnets, J. Magn. Reson. 238 (2014) 52–62, https://doi.org/10.1016/j.jmr.2013.10.026.
[24] C.Z. Cooley, J.P. Stockmann, B.D. Armstrong, M. Sarracanie, M.H. Lev, M.S. Rosen, L.L. Wald, Two-dimensional imaging in a lightweight portable MRI scanner without gradient coils, Magn. Reson. Med. 73 (2015) 872–883, https://doi.org/10.1002/mrm.25147.
[25] C.Z. Cooley, M.W. Haskell, S.F. Cauley, C. Sappo, C.D. Lapierre, C.G. Ha, J.P. Stockmann, L.L. Wald, Design of sparse Halbach magnet arrays for portable MRI using a genetic algorithm, IEEE Trans Magn. 54 (2018), https://doi.org/10.1109/TMAG.2017.2751001.
[26] P.C. McDaniel, C.Z. Cooley, J.P. Stockmann, L.L. Wald, The MR Cap: A single-sided MRI system designed for potential point-of-care limited field-of-view brain imaging, Magn. Reson. Med. (n.d.). https://doi.org/10.1002/mrm.27861.
[27] J. Obungoloch, J.R. Harper, S. Consevage, I.M. Savukov, T. Neuberger, S. Tadigadapa, S.J. Schiff, Design of a sustainable prepolarizing magnetic resonance imaging system for infant hydrocephalus, MAGMA 31 (2018) 665–676, https://doi.org/10.1007/s10334-018-0683-y.
[28] T.R. Ní Mhíocháin, D. Weaire, S.M. McMurry, J.M.D. Coey, Analysis of torque in nested magnetic cylinders, J. Appl. Phys. 86 (1999) 6412–6424, https://doi.org/10.1063/1.371705.
[29] X.N. Xu, D.W. Lu, G.Q. Yuan, Y.S. Han, X. Jin, Studies of strong magnetic field produced by permanent magnet array for magnetic refrigeration, J. Appl. Phys. 95 (2004) 6302–6307, https://doi.org/10.1063/1.1713046.
[30] R. Bjørk, C.R.H. Bahl, A. Smith, N. Pryds, Optimization and improvement of Halbach cylinder design, J. Appl. Phys. 104 (2008) 013910, https://doi.org/10.1063/1.2952537.
[31] F.-A. Fortin, F.-M. De Rainville, M.-A.G. Gardner, M. Parizeau, C. Gagné, DEAP: evolutionary algorithms made easy, J. Mach. Learn. Res. 13 (2012) 2171–2175.
[32] H. Han, R. Moritz, E. Oberacker, H. Waiczies, T. Niendorf, L. Winter, Open source 3D multipurpose measurement system with submillimetre fidelity and

first application in magnetic resonance, Sci. Rep. 7 (2017) 13452, https://doi.org/10.1038/s41598-017-13824-z.
[33] D.S. Webster, K.H. Marsden, Improved apparatus for the NMR measurement of self-diffusion coefficients using pulsed field gradients, Rev. Sci. Instrum. 45 (1974) 1232–1234, https://doi.org/10.1063/1.1686466.
[34] K.C. Chu, B.K. Rutt, Quadrupole gradient coil design and optimization: a printed circuit board approach, Magn. Reson. Med. 31 (1994) 652–659, https://doi.org/10.1002/mrm.1910310611.
[35] R. Turner, A target field approach to optimal coil design, J. Phys. D: Appl. Phys. 19 (1986) L147–L151, https://doi.org/10.1088/0022-3727/19/8/001.
[36] J. Zhen, R. Dykstra, C. Eccles, G. Gouws, S. Obruchkov, A compact Class D RF power amplifier for mobile nuclear magnetic resonance systems, Rev. Sci. Instrum. 88 (2017) 074704, https://doi.org/10.1063/1.4994734.
[37] D.G. Norris, J.M.S. Hutchison, Concomitant magnetic field gradients and their effects on imaging at low magnetic field strengths, Magn. Reson. Imag. 8 (1990) 33–37, https://doi.org/10.1016/0730-725X(90)90209-K.
[38] P.L. Volegov, J.C. Mosher, M.A. Espy, R.H. Kraus, On concomitant gradients in low-field MRI, J. Magn. Reson. 175 (2005) 103–113, https://doi.org/10.1016/j.jmr.2005.03.015.
[39] S. Anand, J.P. Stockmann, L.L. Wald, T. Witzel, A low-cost (<$500 USD) FPGA-based console capable of real-time control, in: Proceedings of the ISMRM 2018, n.d.
[40] C.J. Hasselwander, Z. Cao, W.A. Grissom, gr-MRI: A software package for magnetic resonance imaging using software defined radios, J. Magn. Reson. 270 (2016) 47–55, https://doi.org/10.1016/j.jmr.2016.06.023.
[41] C.A. Michal, A low-cost multi-channel software-defined radio-based NMR spectrometer and ultra-affordable digital pulse programmer, Conc. Magn. Reson. Part B: Magn. Reson. Eng. 48B (2018) e21401, https://doi.org/10.1002/cmr.b.21401.
[42] Y. Hibino, K. Sugahara, Y. Muro, H. Tanaka, T. Sato, Y. Kondo, Simple and low-cost tabletop NMR system for chemical-shift-resolution spectra measurements, J. Magn. Reson. 294 (2018) 128–132, https://doi.org/10.1016/j.jmr.2018.07.003.
[43] M. Nakagomi, M. Kajiwara, J. Matsuzaki, K. Tanabe, S. Hoshiai, Y. Okamoto, Y. Terada, Development of a small car-mounted magnetic resonance imaging system for human elbows using a 0.2 T permanent magnet, J. Magn. Reson. 304 (2019) 1–6, https://doi.org/10.1016/j.jmr.2019.04.017.
[44] J. Hennig, A. Nauerth, H. Friedburg, RARE imaging: a fast imaging method for clinical MR, Magn. Reson. Med. 3 (1986) 823–833, https://doi.org/10.1002/mrm.1910030602.